CrossMark

TESS Asteroseismology of the Known Red-giant Host Stars HD 212771 and HD 203949

Tiago L. Campante[1,2,3] , Enrico Corsaro[4] , Mikkel N. Lund[3,5] , Benoît Mosser[6] , Aldo Serenelli[3,7,8] ,
Dimitri Veras[3,9,10,35] , Vardan Adibekyan[1] , H. M. Antia[11] , Warrick Ball[5,12] , Sarbani Basu[13] ,
Timothy R. Bedding[3,5,14] , Diego Bossini[1] , Guy R. Davies[5,12] , Elisa Delgado Mena[1] , Rafael A. García[15,16] ,
Rasmus Handberg[5] , Marc Hon[17] , Stephen R. Kane[18] , Steven D. Kawaler[3,19] , James S. Kuszlewicz[5,20] , Miles Lucas[19] ,
Savita Mathur[21,22] , Nicolas Nardetto[23] , Martin B. Nielsen[5,12,24] , Marc H. Pinsonneault[3,25] , Sabine Reffert[26] ,
Víctor Silva Aguirre[5] , Keivan G. Stassun[27,28] , Dennis Stello[3,5,14,17] , Stephan Stock[26] , Mathieu Vrard[1] , Mutlu Yıldız[29] ,
William J. Chaplin[3,5,12] , Daniel Huber[3,30] , Jacob L. Bean[31] , Zeynep Çelik Orhan[29] , Margarida S. Cunha[1,2] ,
Jørgen Christensen-Dalsgaard[3,5] , Hans Kjeldsen[5,32] , Travis S. Metcalfe[20,33] , Andrea Miglio[5,12] ,
Mário J. P. F. G. Monteiro[1,2] , Benard Nsamba[1] , Sibel Örtel[29] , Filipe Pereira[1] , Sérgio G. Sousa[1,2] ,
Maria Tsantaki[1] , and Margaret C. Turnbull[34]
[1] Instituto de Astrofísica e Ciências do Espaço, Universidade do Porto, Rua das Estrelas, 4150-762 Porto, Portugal; tiago.campante@astro.up.pt
[2] Departamento de Física e Astronomia, Faculdade de Ciências da Universidade do Porto, Rua do Campo Alegre, s/n, 4169-007 Porto, Portugal
[3] Kavli Institute for Theoretical Physics, University of California, Santa Barbara, CA 93106-4030, USA
[4] INAF—Osservatorio Astrofisico di Catania, via S. Sofia 78, I-95123 Catania, Italy
[5] Stellar Astrophysics Centre (SAC), Department of Physics and Astronomy, Aarhus University, Ny Munkegade 120, DK-8000 Aarhus C, Denmark
[6] LESIA, Observatoire de Paris, Université PSL, CNRS, Sorbonne Université, Université de Paris, 5 place Jules Janssen, F-92195 Meudon, France
[7] Institute of Space Sciences (ICE, CSIC) Campus UAB, Carrer de Can Magrans, s/n, E-08193, Bellaterra, Spain
[8] Institut d'Estudis Espacials de Catalunya (IEEC), C/Gran Capità, 2-4, E-08034, Barcelona, Spain
[9] Centre for Exoplanets and Habitability, University of Warwick, Coventry CV4 7AL, UK
[10] Department of Physics, University of Warwick, Coventry CV4 7AL, UK
[11] Tata Institute of Fundamental Research, Mumbai, India
[12] School of Physics and Astronomy, University of Birmingham, Edgbaston, Birmingham B15 2TT, UK
[13] Department of Astronomy, Yale University, P.O. Box 208101, New Haven, CT 06520-8101, USA
[14] Sydney Institute for Astronomy (SIfA), School of Physics, University of Sydney, Sydney, NSW 2006, Australia
[15] IRFU, CEA, Université Paris-Saclay, F-91191 Gif-sur-Yvette, France
[16] AIM, CEA, CNRS, Université Paris-Saclay, Université Paris Diderot, Sorbonne Paris Cité, F-91191 Gif-sur-Yvette, France
[17] School of Physics, The University of New South Wales, Sydney, NSW 2052, Australia
[18] Department of Earth and Planetary Sciences, University of California, Riverside, CA 92521, USA
[19] Department of Physics and Astronomy, Iowa State University, Ames, IA 50011, USA
[20] Max-Planck-Institut für Sonnensystemforschung, Justus-von-Liebig-Weg 3, D-37077 Göttingen, Germany
[21] Instituto de Astrofísica de Canarias (IAC), E-38205 La Laguna, Tenerife, Spain
[22] Universidad de La Laguna (ULL), Departamento de Astrofísica, E-38206 La Laguna, Tenerife, Spain
[23] Université Côte d'Azur, Observatoire de la Côte d'Azur, CNRS, Laboratoire Lagrange, France
[24] Center for Space Science, NYUAD Institute, New York University Abu Dhabi, P.O. Box 129188, Abu Dhabi, UAE
[25] Department of Astronomy, The Ohio State University, Columbus, OH 43210, USA
[26] Landessternwarte, Zentrum für Astronomie der Universität Heidelberg, Königstuhl 12, D-69117 Heidelberg, Germany
[27] Vanderbilt University, Department of Physics and Astronomy, 6301 Stevenson Center Ln., Nashville, TN 37235, USA
[28] Vanderbilt Initiative in Data-intensive Astrophysics (VIDA), 6301 Stevenson Center Ln., Nashville, TN 37235, USA
[29] Department of Astronomy and Space Sciences, Science Faculty, Ege University, 35100, Bornova, İzmir, Turkey
[30] Institute for Astronomy, University of Hawai'i, 2680 Woodlawn Dr., Honolulu, HI 96822, USA
[31] Department of Astronomy and Astrophysics, University of Chicago, 5640 S. Ellis Ave., Chicago, IL 60637, USA
[32] Institute of Theoretical Physics and Astronomy, Vilnius University, Saulėtekio av. 3, 10257 Vilnius, Lithuania
[33] Space Science Institute, 4750 Walnut Street, Suite 205, Boulder, CO 80301, USA
[34] SETI Institute, Carl Sagan Center for the Study of Life in the Universe, Off-Site: 2801 Shefford Drive, Madison, WI 53719, USA

Abstract

The *Transiting Exoplanet Survey Satellite* (*TESS*) is performing a near all-sky survey for planets that transit bright stars. In addition, its excellent photometric precision enables asteroseismology of solar-type and red-giant stars, which exhibit convection-driven, solar-like oscillations. Simulations predict that *TESS* will detect solar-like oscillations in nearly 100 stars already known to host planets. In this paper, we present an asteroseismic analysis of the known red-giant host stars HD 212771 and HD 203949, both systems having a long-period planet detected through radial velocities. These are the first detections of oscillations in previously known exoplanet-host stars by *TESS*, further showcasing the mission's potential to conduct asteroseismology of red-giant stars. We estimate the fundamental properties of both stars through a grid-based modeling approach that uses global asteroseismic parameters as input. We discuss the evolutionary state of HD 203949 in depth and note the large discrepancy between its asteroseismic mass ($M_* = 1.23 \pm 0.15\,M_\odot$ if on the red-giant branch or $M_* = 1.00 \pm 0.16\,M_\odot$ if in the clump) and the mass quoted in the discovery paper ($M_* = 2.1 \pm 0.1\,M_\odot$), implying a change $>30\%$ in the planet's mass. Assuming HD 203949 to be in the clump, we investigate the planet's past orbital evolution and discuss how it could have avoided engulfment at the tip of the red-giant branch. Finally, HD 212771 was observed by *K2* during its Campaign 3, thus allowing for a preliminary comparison of the asteroseismic performances of *TESS* and

---

[35] STFC Ernest Rutherford Fellow.

K2. We estimate the ratio of the observed oscillation amplitudes for this star to be $A_{\max}^{TESS}/A_{\max}^{K2} = 0.75 \pm 0.14$, consistent with the expected ratio of ~0.85 due to the redder bandpass of *TESS*.

Unified Astronomy Thesaurus concepts: Asteroseismology (73); Exoplanets (498); Evolved stars (481)

1. Introduction

Major advances in stellar interior physics and evolution have recently been made possible by asteroseismology. This has largely been due to the exquisite space-based data made available by Centre National d'Études Spatiales (CNES)/ESA's *CoRoT* (Baglin et al. 2009) and NASA's *Kepler/K2* (Borucki et al. 2010; Koch et al. 2010; Howell et al. 2014) missions. In particular, asteroseismology has vastly benefited the study of solar-type and red-giant stars, which exhibit convection-driven, solar-like oscillations (for a review, see Chaplin & Miglio 2013). The revolution triggered by *CoRoT* and *Kepler/K2* is set to continue over the coming decade, with NASA's *TESS* (Ricker et al. 2015) and ESA's *PLATO* (Rauer et al. 2014) missions expected to raise the number of known solar-like oscillators by up to two orders of magnitude (Huber 2018).

Fueled by the wealth of high-quality seismic data, the past few years have witnessed an ever-growing effort being devoted to the development of novel techniques for the estimation of fundamental stellar properties. The focus has been placed on uniform data analysis (e.g., Davies et al. 2016; Lund et al. 2017b) and stellar modeling (e.g., Serenelli et al. 2017; Silva Aguirre et al. 2017; Nsamba et al. 2018) strategies, as well as on state-of-the-art optimization procedures that make use of individual oscillation frequencies (e.g., Metcalfe et al. 2010; Mathur et al. 2012; Silva Aguirre et al. 2015; Rendle et al. 2019).

These techniques make it possible to estimate precise properties of large numbers of field stars, for which such information is sparse. As a result, asteroseismology is having a profound impact on modern astrophysics, notably on the field of exoplanetary science (Campante et al. 2018). Characterization of exoplanet-host stars via asteroseismology allows for unmatched precision in the absolute properties of their planets (Huber et al. 2013a; Ballard et al. 2014; Campante et al. 2015; Silva Aguirre et al. 2015; Lundkvist et al. 2016). Furthermore, asteroseismology enables constraints on the spin–orbit alignment of exoplanet systems (Chaplin et al. 2013; Huber et al. 2013b; Campante et al. 2016a; Kamiaka et al. 2019) as well as statistical inferences on orbital eccentricities via asterodensity profiling (Sliski & Kipping 2014; Van Eylen & Albrecht 2015; Van Eylen et al. 2019).

The *Transiting Exoplanet Survey Satellite* (*TESS*) is performing a near all-sky survey for planets that transit bright stars. Moreover, its excellent photometric precision, combined with its fine time sampling and long intervals of uninterrupted observations, enables asteroseismology of solar-like oscillators (Campante et al. 2016b; Schofield et al. 2019). In particular, simulations predict that *TESS* will detect solar-like oscillations in nearly 100 solar-type and red-giant stars already known to host planets (Campante et al. 2016b).

In this paper, we present an asteroseismic analysis of the evolved known hosts HD 212771 and HD 203949, both systems having a long-period planet detected through the radial-velocity (RV) method. These are the first detections of oscillations in previously known exoplanet-host stars by *TESS* and follow the discovery of the first planet transiting a star in

which oscillations could be measured (TOI-197 or *TESS* Object of Interest 197; Huber et al. 2019).

HD 212771 (TIC 12723961, HIP 110813) is a bright (with apparent *TESS* magnitude $T = 6.75$), spectroscopically classified subgiant (G8 IV; Houk & Smith-Moore 1988), being among the targets of the RV planet survey of Johnson et al. (2007). It hosts a Jovian planet with minimum mass $M_p \sin i = 2.3 \pm 0.4\,M_J$ in a 373.3 days orbit (Johnson et al. 2010). HD 212771 was subsequently observed by *K2* in short cadence during its Campaign 3, spanning a total of ~69 days. This allowed estimation of its fundamental properties through a grid-based modeling approach that used global asteroseismic parameters, complementary spectroscopy and a parallax-based luminosity as input (Campante et al. 2017; North et al. 2017).

HD 203949 (TIC 129649472, HIP 105854) is a bright ($T = 4.75$), spectroscopically classified giant (*K2* III; Houk 1982). A massive planet ($M_p \sin i = 8.2 \pm 0.2\,M_J$) was discovered in a 184.2 days circular ($e = 0.02 \pm 0.03$) orbit around HD 203949 by Jones et al. (2014) as part of the EXoPlanets aRound Evolved StarS project (Jones et al. 2011).

The rest of this paper is organized as follows. In Section 2, we present the available observational data (including the *TESS* photometry). This is followed by an asteroseismic analysis (Section 3) and the estimation of fundamental stellar properties through a grid-based modeling approach (Section 4). Finally, we discuss our results in Section 5 and provide an outlook in Section 6.
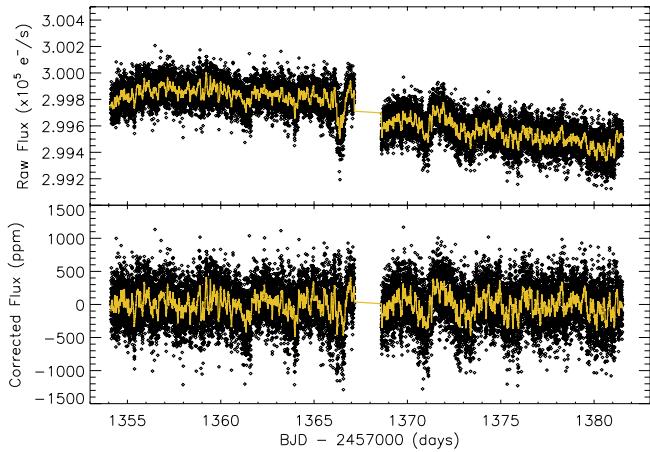
2. Observations

2.1. TESS *Photometry*

TESS observed HD 212771 and HD 203949 in 2 minutes cadence over 27.4 days during Sectors 2 and 1 of Cycle 1, respectively. Both targets were part of a larger cohort of 79 "fast-track" targets that were processed using a special version (Handberg & Lund 2018) of the *TESS* Asteroseismic Science Operations Center[36] (TASOC; Lund et al. 2017a) photometry pipeline.[37] Starting from calibrated target pixel files, aperture photometry was conducted following a procedure similar to the one adopted in the K2P² pipeline (Lund et al. 2015), originally developed to generate light curves from data collected by *K2*. The extracted light curves were subsequently corrected for systematic effects using the Kepler Asteroseismic Science Operations Center (KASOC) filter (Handberg & Lund 2014).

Figure 1 shows the light curves of HD 212771 (left panel) and HD 203949 (right panel) produced by the TASOC pipeline. Both light curves have high duty cycles (~98% and ~94%, respectively), displaying a gap midway through (due to the data downlink) that separates the two spacecraft orbits in each sector. A 2.5 days periodicity can be seen, especially in the bottom left subpanel, caused by the spacecraft's angular momentum dumping cycle. Moreover, a region of large jitter can be seen in the right panel toward the end of the sector, a

---

[36] https://tasoc.dk/
[37] https://github.com/tasoc

Figure 1. Light curves of HD 212771 (left panel) and HD 203949 (right panel) produced by the TASOC photometry pipeline. In each panel, raw (top) and corrected (bottom) 2 minutes cadence light curves are displayed. A smoothed—using a 1 hr (HD 212771) and 10 minutes (HD 203949) boxcar filters—version of the light curve is depicted by a yellow curve in each subpanel.

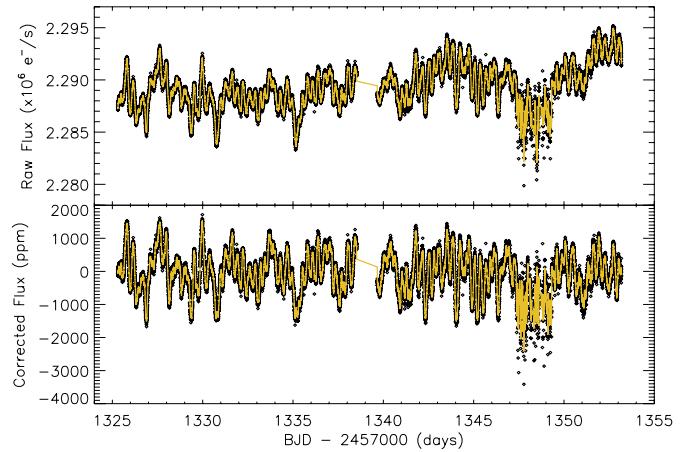feature common to Sector 1 pointings (Handberg & Lund 2018).

2.2. High-resolution Spectroscopy

We adopt the atmospheric parameters and elemental abundances obtained for HD 212771 by Campante et al. (2017), which are based on the analysis of a high-quality Fiber-fed Extended Range Optical Spectrograph (FEROS) spectrum (see Table 1).

Particular care must, however, be taken regarding HD 203949, because use of the model-independent scaling relation $g \propto \nu_{max} T_{eff}^{1/2}$ (Brown et al. 1991; Kjeldsen & Bedding 1995; Belkacem et al. 2011), where ν_{max} is the frequency of maximum oscillation amplitude (see Section 3.1), leads to an initial estimate of the surface gravity ($\log g \sim 2.4$) that is significantly lower than the spectroscopic value quoted in the discovery paper ($\log g = 2.94 \pm 0.20$; Jones et al. 2011, 2014).

Therefore, we instead adopt the spectroscopic parameters listed for HD 203949 in the SWEET-Cat catalog[38] (Santos et al. 2013), whose $\log g$ is compatible with the one inferred from asteroseismology. These are based on the analysis of a high-resolution ($R \sim 100{,}000$) Ultraviolet and Visual Échelle Spectrograph (UVES) spectrum (for details, see Sousa et al. 2018) and are listed in Table 2. Analysis of a lower-resolution ($R \sim 48{,}000$) FEROS spectrum by the same authors, albeit considering a larger number of iron lines, led to fully consistent spectroscopic parameters.

We conducted a detailed abundance analysis of HD 203949 based on both the UVES and FEROS spectra, following the methodology described by Adibekyan et al. (2012, 2015a). Abundances derived from the two spectra are consistent within 1σ, with UVES-based results being slightly more precise. Our analysis shows that HD 203949 has a chemical composition typical of a thin-disk, metal-rich K giant (e.g., Adibekyan et al. 2015b; Jofré et al. 2015). The star shows enhancement in Na and Al relative to iron ([Na/Fe] $= 0.22 \pm 0.13$ dex and [Al/Fe] $= 0.25 \pm 0.12$ dex based on the UVES spectrum), typical of evolved stars (e.g., Adibekyan et al. 2015b). Finally, we computed the relative abundance of α elements as the

Table 1
Stellar Parameters for HD 212771

Parameter	Value	Source
Basic Properties		
TIC	12723961	1
Hipparcos ID	110813	2
TESS Mag.	6.75	1
Sp. Type	G8 IV	3
Spectroscopy		
T_{eff} (K)	5065 ± 75	4
[Fe/H] (dex)	-0.10 ± 0.10	4
[α/Fe] (dex)	0.06 ± 0.05[a]	4
$\log g$ (cgs)	3.37 ± 0.17	4
SED and *Gaia* DR2 Parallax		
A_V	0.04 ± 0.04	5
F_{bol} (erg s^{-1} cm^{-2})	$(3.06 \pm 0.14) \times 10^{-8}$	5
R_* (R$_\odot$)	4.44 ± 0.13	5
L_* (L$_\odot$)	11.67 ± 0.57	5
π (mas)	9.050 ± 0.055[b]	6
SBCR		
θ (mas)	0.375 ± 0.003	5
R_* (R$_\odot$)	4.45 ± 0.07	5
Asteroseismology		
$\Delta\nu$ (μHz)	16.25 ± 0.19	5
ν_{max} (μHz)	226.6 ± 9.4	5
$\Delta\Pi_1$ (s)	85.3 ± 0.3	5
M_* (M$_\odot$)	1.42 ± 0.07	5
R_* (R$_\odot$)	4.61 ± 0.09	5
ρ_* (gcc)	0.02048 ± 0.00050	5
$\log g$ (cgs)	3.263 ± 0.010	5
t (Gyr)	2.90 ± 0.47	5

Notes.
[a] The uncertainty (0.02) reported in (4) is not correct.
[b] Adjusted for the systematic offset of Stassun & Torres (2018).
References. (1) Stassun et al. (2018b), (2) van Leeuwen (2007), (3) Houk & Smith-Moore (1988), (4) Campante et al. (2017), (5) this work, (6) Gaia Collaboration et al. (2018).

---

[38] https://www.astro.up.pt/resources/sweet-cat/

Parameter	Value	Source
Basic Properties		
TIC	129649472	1
Hipparcos ID	105854	2
TESS Mag.	4.75	1
Sp. Type	*K2* III	3
Spectroscopy		
$T_{\rm eff}$ (K)	4618 ± 113	4
[Fe/H] (dex)	0.17 ± 0.07	4
[α/Fe] (dex)	0.07 ± 0.09	5
$\log g$ (cgs)	2.36 ± 0.28	4
SED and Gaia DR2 Parallax		
A_V	0.13 ± 0.10	5
$F_{\rm bol}$ (erg s^{-1} cm^{-2})	$(2.27 \pm 0.22) \times 10^{-7}$	5
$R_\star$ ($R_\odot$)	10.30 ± 0.51	5
$L_\star$ ($L_\odot$)	43.34 ± 4.27	5
π (mas)	12.77 ± 0.13[a]	6
SBCR		
θ (mas)	1.284 ± 0.011	5
$R_\star$ ($R_\odot$)	10.8 ± 1.6	5
Asteroseismology[b]		
$\Delta\nu$ (μHz)	4.10 ± 0.14	5
$\nu_{\rm max}$ (μHz)	31.6 ± 3.2	5
$\Delta\Pi_1$ (s)	…	…
$M_\star$ ($M_\odot$)	$1.23 \pm 0.15/1.00 \pm 0.16$	5
$R_\star$ ($R_\odot$)	$10.93 \pm 0.54/10.34 \pm 0.55$	5
$\rho_\star$ (gcc)	$0.00134 \pm 0.00010/0.00130 \pm 0.00011$	5
$\log g$ (cgs)	$2.453 \pm 0.027/2.415 \pm 0.044$	5
t (Gyr)	$6.45 \pm 2.79/7.29 \pm 3.06$	5

Notes.
[a] Adjusted for the systematic offset of Stassun & Torres (2018).
[b] Fundamental stellar properties are provided assuming that the star is either on the RGB or in the clump, respectively (see Section 5.2).
References. (1) Stassun et al. (2018b), (2) van Leeuwen (2007), (3) Houk (1982), (4) Sousa et al. (2018), (5) this work, (6) Gaia Collaboration et al. (2018).

unweighted mean of the Mg, Si, Ca, and Ti abundances derived from the UVES spectrum, resulting in [α/Fe] $= 0.07 \pm 0.09$ dex.

2.3. Broadband Photometric Spectral Energy Distribution

We fitted the spectral energy distributions (SEDs) of both stars using broadband photometry to determine empirical constraints on the stellar radii and luminosities, following the method described in Stassun & Torres (2016) and Stassun et al. (2018a). The available broadband photometry in published all-sky catalogs (i.e., APASS, 2MASS and *Wide-field Infrared Survey Explorer*) provides coverage over the wavelength range ≈ 0.4–$22\,\mu$m. For each star, we fitted a standard Kurucz (2013) stellar atmosphere model, selected according to the spectroscopically determined $T_{\rm eff}$, $\log g$, and [Fe/H] (see Section 2.2). With these constraints fixed, the remaining free parameter in the fit was the extinction, A_V, which we limited to the maximum for the line of sight from the dust maps of Schlegel

et al. (1998). Finally, we integrated the (non-reddened) SED to obtain the bolometric flux at Earth ($F_{\rm bol}$) which, with the $T_{\rm eff}$ and the *Gaia* DR2 distance (adjusted for the systematic offset of Stassun & Torres 2018), gives the stellar radius.

The best-fit parameters for HD 212771, with reduced $\chi^2 = 4.7$, are: $A_V = 0.04 \pm 0.04$, $F_{\rm bol} = (3.06 \pm 0.14) \times 10^{-8}$ erg s^{-1} cm^{-2}, resulting in $R_\star = 4.44 \pm 0.13$ $R_\odot$ and $L_\star = 11.67 \pm 0.57$ $L_\odot$. For HD 203949, the best-fit parameters, with reduced $\chi^2 = 3.7$, are: $A_V = 0.13 \pm 0.10$, $F_{\rm bol} = (2.27 \pm 0.22) \times 10^{-7}$ erg s^{-1} cm^{-2}, resulting in $R_\star = 10.30 \pm 0.51$ $R_\odot$ and $L_\star = 43.34 \pm 4.27$ $L_\odot$. The derived luminosities will be used in Section 4 as input to the grid-based modeling.

2.4. Surface Brightness–Color Relation (SBCR)

Pietrzyński et al. (2019) derived the distance to the Large Magellanic Cloud with a 1% precision using eclipsing binaries as distance indicators. In order to achieve such precision, they used a dedicated SBCR based on the observation of 48 red-clump (RC) stars with the PIONIER/VLTI instrument (Gallenne et al. 2018). We used this relation to place empirical constraints on the angular diameters and linear radii of HD 212771 and HD 203949.
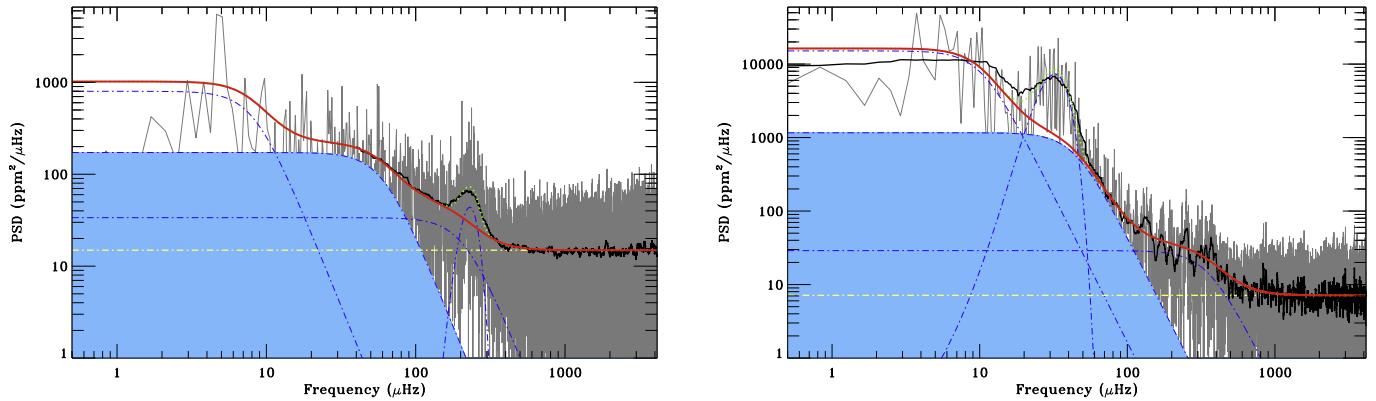
For HD 212771, considering $V = 7.60 \pm 0.01$ (Høg et al. 2000), $K = 5.50 \pm 0.02$ (Cutri et al. 2003), $A_V = 0.005$ (using the Stilism dust map; Lallement et al. 2014; Capitanio et al. 2017), and $A_K = 0.089 A_V$ (Nishiyama et al. 2009), we obtained (using Equation (2) of Pietrzyński et al. 2019) a limb-darkened angular diameter of $\theta = 0.375 \pm 0.003$ mas. The quoted uncertainty (0.8%) arises from the rms scatter (0.018 mag) of the SBCR in Pietrzyński et al. (2019). Using the *Gaia* DR2 parallax, we then derived a stellar radius of $R_\star = 4.45 \pm 0.04\,R_\odot$. We must, however, also consider the source of uncertainty associated with the 2MASS infrared photometry (0.02 mag), which corresponds to an additional uncertainty in the radius of $0.05\,R_\odot$. We thus finally obtained $R_\star = 4.45 \pm 0.07\,R_\odot$. Applying the same procedure to HD 203949 ($V = 5.62 \pm 0.01$, $K = 2.99 \pm 0.24$, and $A_V = 0.004$), we obtained a limb-darkened angular diameter of $\theta = 1.284 \pm 0.011$ mas and a stellar radius of $R_\star = 10.8 \pm 1.6\,R_\odot$ (after taking into account the exceptionally large uncertainty of 0.24 mag in the infrared photometry). The derived stellar radii are consistent with those obtained from the SED analysis.

3. Asteroseismology

Figure 2 shows the power spectra of HD 212771 (left panel) and HD 203949 (right panel) computed based on the TASOC light curves. These reveal clear power excesses due to solar-like oscillations at $\sim 230\,\mu$Hz and $\sim 30\,\mu$Hz, respectively. Figure 3 shows the échelle diagrams of the smoothed power spectra of HD 212771 (left panel) and HD 203949 (right panel).

3.1. Global Oscillation Parameters

The large frequency separation, $\Delta\nu$, and frequency of maximum oscillation amplitude, $\nu_{\rm max}$, were measured based on the analysis of the above power spectra. A range of well-tested and complementary automated methods were used in the analysis (Huber et al. 2009, 2011; Mosser & Appourchaux 2009; Mathur et al. 2010; Mosser et al. 2011; Corsaro &

Figure 2. Power spectral density (PSD) of HD 212771 (left panel) and HD 203949 (right panel). The PSD is shown in gray (with a heavily smoothed version in black). The solid red curve is a fit to the background, consisting of three Harvey-like profiles (blue dotted–dashed curves) plus white noise (yellow horizontal dotted–dashed line). A global fit to the oscillation power excess (blue dotted–dashed Gaussian curve) and the background is visible at ∼230 μHz (HD 212771) and ∼30 μHz (HD 203949) as a dotted green curve.

De Ridder 2014; Corsaro et al. 2015; Davies & Miglio 2016; Campante 2018; Yu et al. 2018), which have previously been extensively applied to data from *Kepler*/K2 (e.g., Hekker et al. 2011; Verner et al. 2011). Returned values were subject to a preliminary step which involved the rejection of outliers following Peirce's criterion (Peirce 1852; Gould 1855). For each star, we finally adopted the values of $\Delta\nu$ and $\nu_{\max}$ corresponding to the smallest normalized rms deviation about the median, considering both parameters simultaneously (i.e., both parameters originate from the same source/method). Uncertainties were recalculated by adding in quadrature the corresponding formal uncertainty and the standard deviation of the parameter estimates returned by all methods. Consolidated values for $\Delta\nu$ and $\nu_{\max}$ are given in Tables 1 and 2.

3.2. HD 212771: Asymptotic Mixed-mode Pattern and Rotation

Mixed modes in HD 212771 were analyzed following the method of Mosser et al. (2015), which revealed the signature of the period spacing, $\Delta\Pi_1$. Its value, computed as in Vrard et al. (2016), is $\Delta\Pi_1 = 84.3 \pm 1.6$ s. A fit of the mixed-mode pattern provides a more refined value of the period spacing, $\Delta\Pi_1 = 85.3 \pm 0.3$ s, and a coupling factor $q = 0.19 \pm 0.03$. Such values are in agreement with the general trends found in *Kepler* data for stars on the red-giant branch (RGB; Mosser et al. 2017). This is supported by the star's location in a $\Delta\Pi_1$–$\Delta\nu$ diagram (see Figure 1 of Mosser et al. 2014). We thus reclassify HD 212771 as a low-luminosity RGB star based on asteroseismology.

Since the mixed-mode pattern also revealed rotational multiplets, we next performed an analysis of the rotational splittings of dipole mixed modes (based on a power spectrum oversampled by a factor of 4). In a preliminary step, rotational splittings were identified using an asymptotic mixed-mode pattern modulated by a core rotation rate of 400 nHz. Comparison of the spectrum with the asymptotic fit revealed 13 mixed modes with a height-to-background ratio larger than 5, among which 8 are forming rotational doublets, corresponding to the mixed-mode orders −40, −38, −35, and −34 (see Figure 4 and Table 3). The remaining components were identified as being $|m| = 1$ modes. The absence of any significant dipole mode with azimuthal order $m = 0$ is in favor of a star seen edge-on. As shown by Kamiaka et al.
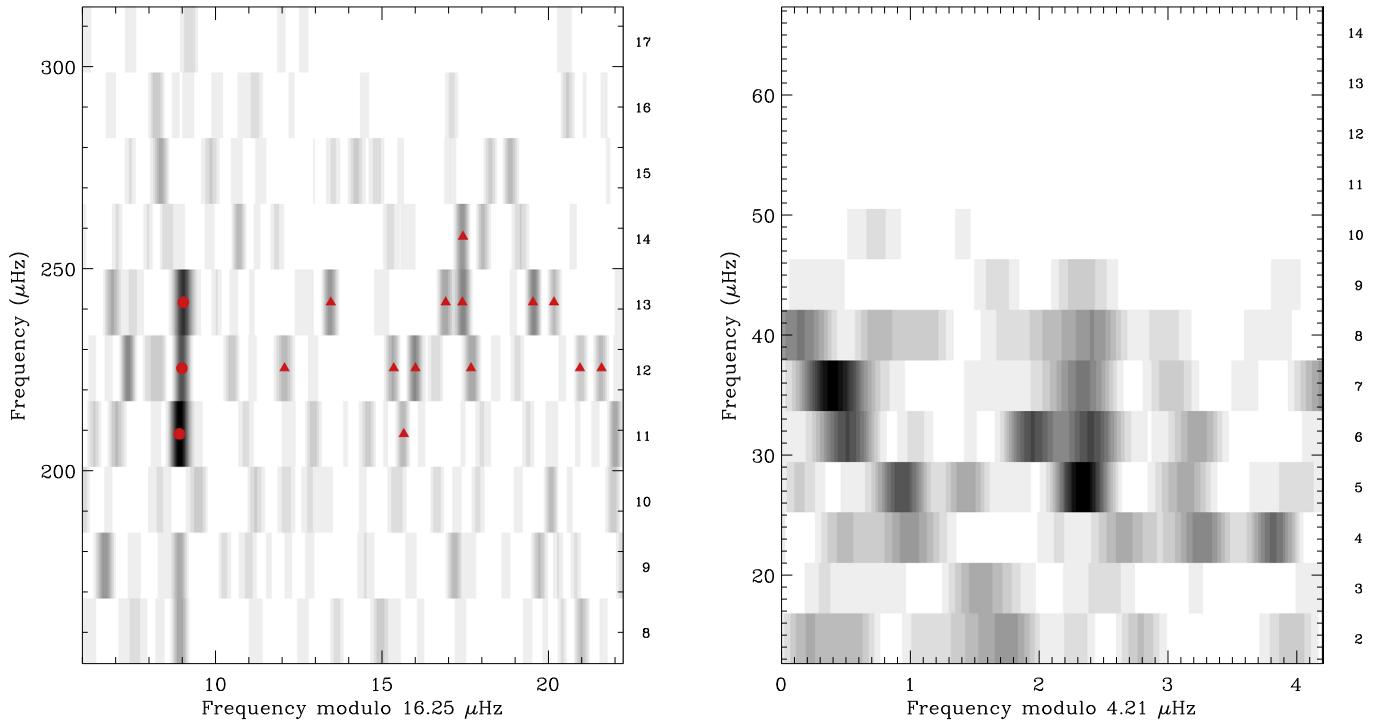
(2018), deriving a reliable and precise value of the stellar inclination is difficult when the height-to-background ratio of the modes is small. Based on the observed height-to-background ratio of the rotational doublets, an inclination angle larger than 75° is to be expected, consistent with a potentially aligned transiting system.

To derive the mean core rotation, rotational splittings were expressed as a function of ζ, which describes the relative contribution of the inner radiative region to the mode inertia (Goupil et al. 2013; Deheuvels et al. 2014; Mosser et al. 2018). This method allowed us to derive the individual splitting of each component of the multiplet, with the total rotational splitting between the $m = -1$ and $m = +1$ components being split according to the respective ζ coefficients of each mode. We further assumed that the uncertainties of the unresolved dipole mixed modes cannot be less than half the frequency resolution. The method then returns a nominal, albeit imprecise, mean core rotation of $\delta\nu_{\rm rot} = 354 \pm 151$ nHz.
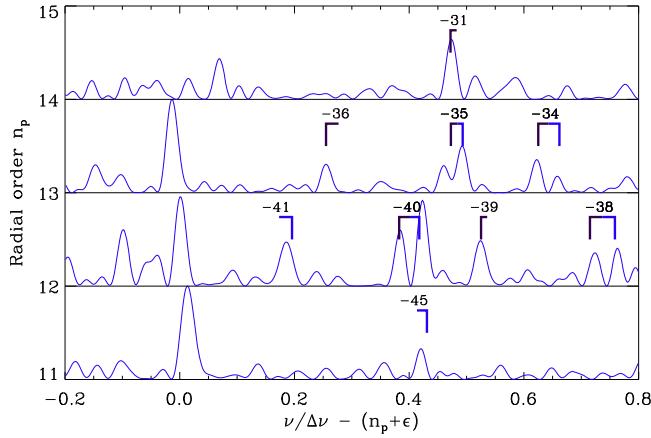
3.3. HD 203949: What Causes the Second Power Excess?

In order to properly fit the background power spectral density (PSD) of HD 203949, three Harvey-like profiles were required, as determined from a Bayesian model comparison using DIAMONDS (Corsaro & De Ridder 2014). One of the profiles in this preferred model has, however, a timescale and amplitude that do not conform with expectations based on the measured $\nu_{\max}$ (e.g., Kallinger et al. 2014), with a "knee"[39] at ∼300 μHz (see right panel of Figure 2). We suspect that this second power hump is caused by jitter in the *TESS* data that remains after applying the KASOC filter, which is particularly pronounced during the 1347–1350 days period of poor space-craft tracking (see right panel of Figure 1). We note that the power hump is also evident from the simple aperture photometry (SAP) delivered by the *TESS* Science Processing Operations Center (SPOC; Jenkins et al. 2016), while it is largely removed in the co-trended Presearch Data Conditioning SAP (PDCSAP)—the oscillation signal in the PDCSAP data is,

---

[39] In the interest of reproducibility, we provide the fitted parameters of the three Harvey-like profiles (for the adopted functional form and a definition of the parameters $\{a_i, b_i\}$, see Equation (4) of Corsaro et al. 2017). For HD 203949, one has $\{a_1, a_2, a_3\} = \{414^{+44}_{-45}, 239^{+44}_{-62}, 106^{+4}_{-4}\}$ ppm and $\{b_1, b_2, b_3\} = \{10.2^{+1.4}_{-1.6}, 44.2^{+7.7}_{-8.9}, 352^{+16}_{-15}\}$ μHz. For HD 212771, one has $\{a_1, a_2, a_3\} = \{85.6^{+10.6}_{-11.3}, 107^{+8}_{-7}, 88.7^{+8.0}_{-7.1}\}$ ppm and $\{b_1, b_2, b_3\} = \{8.25^{+1.39}_{-1.74}, 60.1^{+16.7}_{-9.0}, 210^{+37}_{-20}\}$ μHz.

Figure 3. Grayscale échelle diagram of the smoothed PSD of HD 212771 (left panel) and HD 203949 (right panel). The pressure radial order, n_p, is indicated along the right y-axis. Identified individual modes for HD 212771 (see Figure 4 and Table 3) are marked with red circles ($\ell = 0$, radial modes) and red triangles ($\ell = 1$, dipole modes). A proxy for $\Delta\nu$ of 4.21 μHz (within errors of the quoted value in Table 2) is used in the right panel to enhance the vertical alignment of the ridges.

Figure 4. Mixed-mode pattern of HD 212771. The PSD along each pressure radial order, n_p, is shown as a function of reduced frequency, $\nu/\Delta\nu - (n_p + \epsilon)$, where ϵ is a phase shift sensitive to the properties of the near-surface layers of the star. The three prominent radial modes have a reduced frequency close to 0 (modulated by acoustic glitches). The mixed-mode orders, n_m, are indicated, with color coding the azimuthal order ($m = -1$ in dark purple and $m = 1$ in blue; see Table 3).

Table 3
Low-degree Oscillation Pattern of HD 212771

n_p	ℓ	m	n_m	ζ	ν_{as} (μHz)	ν_{obs} (μHz)	h
11	0	0	⋯	⋯	203.34	203.92	20.7
11	1	1	−45	0.718	210.84	210.67	8.1
12	0	0	⋯	⋯	219.73	220.27	14.8
12	1	1	−41	0.934	223.49	223.34	6.2
12	1	−1	−40	0.775	226.58	226.62	8.2
12	1	1	−40	0.680	227.16	227.27	12.1
12	1	−1	−39	0.441	228.94	228.94	7.6
12	1	−1	−38	0.884	232.08	232.21	5.9
12	1	1	−38	0.910	232.80	232.86	5.8
13	0	0	⋯	⋯	236.21	236.55	23.9
13	1	−1	−36	0.901	241.01	240.98	10.1
13	1	−1	−35	0.445	244.61	244.43	7.5
13	1	1	−35	0.394	244.95	244.93	11.7
13	1	−1	−34	0.724	247.13	247.05	9.9
13	1	1	−34	0.802	247.74	247.68	5.1
14	1	−1	−31	0.444	261.14	261.20	13.4

Note. Each mode is labeled according to its pressure radial order, n_p, degree, ℓ, and azimuthal order, m; mixed modes are further characterized by their mixed-mode order, n_m, and ζ coefficient. The asymptotic guess frequency, ν_{as}, is given, as well as the observed frequency, ν_{obs}, and height-to-background ratio, h. The Doppler shift of the observed frequencies due to the line-of-sight motion (Davies et al. 2014) is significant for both stars in this study (no correction has been applied here). We note, however, that this has a negligible effect on the analysis performed in Section 3.1.

however, of lower quality than the one present in the TASOC data.

Support for the hypothesis of jitter causing the second power hump comes from the MOM_CENTR2 data delivered by SPOC, which gives the flux-centroid along rows on the charge-coupled device (CCD). The PSD of this centroid time series shows a clear excess at ∼300 μHz. Jitter at this frequency would cause a variation in the flux from inter/intra pixel sensitivity and from flux exiting/entering the aperture. We found that adopting a larger aperture than the one set by the TASOC pipeline made the power hump disappear, but at the cost of a degraded oscillation signal. Furthermore, the hypothesis that this feature

is instrumental in nature is reinforced by noting that the power hump nearly vanishes if the 1347–1350 days data are omitted from the PSD calculation, and that the short-cadence light curve for the nearby star TIC 129679884 shows the same effect.

Since the power hump is well separated in frequency from the power excess due to oscillations, we could account for it in the fitted background without affecting the analysis of the oscillations.

4. Estimation of Fundamental Stellar Properties

Fundamental stellar properties can be estimated by comparing global asteroseismic parameters and complementary spectroscopic and astrometric data to the outputs of stellar evolutionary models. We used a number of independent grid-based pipelines in this work (Stello et al. 2009; Basu et al. 2010, 2012; Metcalfe et al. 2010; Gai et al. 2011; Rodrigues et al. 2014, 2017; Silva Aguirre et al. 2015; Yıldız et al. 2016; Serenelli et al. 2017), whereby observables are matched to well-sampled grids of stellar evolutionary tracks. The diversity of grids and optimization procedures employed implicitly account for the impact of using different stellar models— covering a range of input physics—and analysis methodologies on the final estimates. The adopted set of observables consists of $\{\Delta\nu,\ \nu_{max},\ [Fe/H],\ T_{eff},\ L_*\}$. Given the negligible α enhancement (see Tables 1 and 2), we have neglected its effect.

We provide consolidated values from grid-based modeling for the stellar mass, M_*, radius, R_*, mean density, ρ_*, surface gravity, $\log g$, and age, t, in Tables 1 and 2. To properly account for systematics, values returned by the several pipelines were subject to the same procedure as described in Section 3.1 (i.e., single source/method), except that no preliminary outlier rejection step has now been applied.

The properties estimated for HD 212771 in this work are consistent with those estimated by Campante et al. (2017) based on K2 asteroseismology. As noted by those authors, the derived asteroseismic mass places HD 212771 just within the *retired A star* category,[40] being significantly larger than the value reported in the discovery paper (see also North et al. 2017).

Regarding HD 203949, we provide fundamental properties assuming that the star is either on the RGB or in the clump, deferring a discussion of its evolutionary state until Section 5.2. We note the large discrepancy between both asteroseismic masses derived in this work and the mass quoted in the discovery paper ($M_* = 2.1 \pm 0.1\ M_\odot$; Jones et al. 2014). Jones et al. (2014) identified HD 203949 as a post-RGB star. Their large mass determination can, to a large extent, be ascribed to the surface gravity adopted, $\log g = 2.94 \pm 0.20$, consistent with stars in the secondary clump and hence masses $\gtrsim 2\ M_\odot$. Under the assumption that HD 203949 is in the clump, the lower seismic gravity (see Table 2) is consistent with that of a typical RC star, ruling out a large mass. We stress here that asteroseismology can be used to accurately and robustly determine surface gravities for red giants, with systematic offsets of only a few percent (Pinsonneault et al. 2018).

This large mass discrepancy calls for a revision of both the planet's semimajor axis and minimum mass. By assuming an RV semi-amplitude of $178.1 \pm 10.0\ m\,s^{-1}$ and an orbital period of 184.2 ± 0.5 days (Jones et al. 2014), we find that in the RGB scenario, $a = 0.68 \pm 0.03$ au and $M_p \sin i = 5.7 \pm 0.6\ M_J$, whereas in the clump scenario, $a = 0.63 \pm 0.04$ au and $M_p \sin i = 5.0 \pm 0.6\ M_J$. In both cases, the parameters were derived assuming a circular orbit, in line with the observed eccentricity. The revision of the planet's properties thus implies a change >30% in its estimated mass.

5. Discussion

5.1. Asteroseismic Performance: TESS versus Kepler/K2

HD 212771 was observed by K2 in short cadence (Campante et al. 2017; North et al. 2017), which enabled its asteroseismic investigation. Here, we compare the asteroseismic performances of K2 and TESS by assessing the ratio of the observed maximum oscillation amplitudes for this star, i.e., $A_{max}^{TESS}/A_{max}^{K2}$.

The absolute calibration of the oscillation amplitudes depends on the instrument's bandpass. TESS has a redder bandpass than Kepler/K2, meaning observed amplitudes are expected to be lower in the TESS data by a factor of ~0.85 (Campante et al. 2016b). Based on a blackbody approximation, Lund (2019) finds this factor to be slightly lower, i.e., ~0.83–0.84 on average within the T_{eff} range considered in that study. We measured the maximum oscillation amplitude per radial mode, A_{max}, following the method introduced by Kjeldsen et al. (2005, 2008), which involves determining the peak of the heavily smoothed, background-corrected amplitude oscillation envelope having accounted for the (bandpass-dependent) effective number of modes per radial order.[41] This yielded $A_{max}^{TESS} = 12.8 \pm 2.3$ ppm and $A_{max}^{K2} = 17.1 \pm 0.9$ ppm, resulting in a ratio $A_{max}^{TESS}/A_{max}^{K2} = 0.75 \pm 0.14$, consistent with the expected ratio.

We caution the reader that the estimated $A_{max}^{TESS}/A_{max}^{K2}$ is prone to unaccounted biases due to the stochastic nature of the oscillations (e.g., Arentoft et al. 2019), especially when considering the short time coverage compared to the lifetime of the modes as well as the non-contemporaneity of the TESS and K2 data sets. Moreover, the absolute values of A_{max}^{TESS} and A_{max}^{K2}, taken individually, are also subject to biases arising from the choice of background model. Their ratio, however, can be more accurately estimated if both values are computed assuming the same functional form for the background model, which has been done here. Despite the above, this preliminary, single-point estimate of $A_{max}^{TESS}/A_{max}^{K2}$ provides support for the predicted yield of solar-like oscillators using TESS's 2 minutes cadence observations (Schofield et al. 2019).

5.2. On the Evolutionary State of HD 203949: RGB versus RC

RC stars, i.e., cool He-core burning stars, occupy a confined parameter space in the $\Delta\Pi_1$–$\Delta\nu$ diagram around 300 s and 4.1 μHz (Mosser et al. 2012). Although the $\Delta\nu$ value measured for HD 203949 is consistent with it being an RC star, the low-frequency resolution of the power spectrum hinders a measurement of $\Delta\Pi_1$. This in turn prevents a definitive classification of its evolutionary state from being made based on the $\Delta\Pi_1$–$\Delta\nu$ diagram, due to the underlying degeneracy for $\Delta\nu \lesssim 10\ \mu$Hz (e.g., Mosser et al. 2014). In an attempt to assess the evolutionary state of HD 203949, we have thus conducted a number of analyses, which we summarize below.

Machine learning classification. We employed the deep learning method of Hon et al. (2017, 2018), which efficiently

---

[40] RV planet surveys rely on evolved stars for a sample of intermediate-mass stars ($M_* \gtrsim 1.5\ M_\odot$; so-called retired A stars), which are more amenable to RV observations than their main-sequence counterparts.

[41] We used the same K2 light curve as in Campante et al. (2017) in our analysis.

classifies the evolutionary state of oscillating red giants by recognizing visual features in their asteroseismic power spectra. A test set accuracy of 93.2% has been reported when applying the classifier to a 27 days photometric time series (Hon et al. 2018). Application of this method to the power spectrum of HD 203949 returns a probability of it being an RC star of $p \sim 0.6$, having taken into account the effect of detection bias in the training set.

Alternatively, we have made use of Clumpiness (J. Kuszlewicz et al. 2019, in preparation). Clumpiness uses a handful of well-engineered features and a gradient boosting algorithm (xgboost; Chen & Guestrin 2016) to classify stars as RGB or RC (or even as possible main-sequence stars observed in long cadence) in the time domain. These features include the median absolute deviation (MAD) from the median of the time series flux, the number of zero crossings, a measure of the stochasticity following Kedem & Slud (1981, 1982) and Bae et al. (1996), the MAD of the first differences, and, to complement the time series features, the K-band absolute magnitude is also included, which is computed using distances from Bailer-Jones et al. (2018) and a 3D dust map from Green et al. (2015). Across a range of time series lengths, from 27 days up to 4 years, the classifier maintains an accuracy of approximately 92%. Computing the features for HD 203949, the classifier returns a probability of 0.6 of it being in the RC.

Grid-based modeling. For a given set of seismic and spectroscopic observational constraints, the evolutionary state of HD 203949 can also be assessed from the results of grid-based modeling. We have thus performed two separate analyses, each assuming as prior information a specific evolutionary state, i.e., RGB or RC. We found that the probability of HD 203949 being an RC star is 75 times greater than it being an RGB star (or $p = 0.99$), as determined by the ratio of the overall posterior probabilities of both scenarios. Interpreting this in terms of a Bayes' factor provides very strong evidence in support of the RC scenario given the adopted set of seismic and spectroscopic constraints. We looked into which observational constraints are driving this result by analyzing their posterior distributions. RC stellar models reproduce all constraints very well, while RGB models cannot simultaneously fit the effective temperature and metallicity for stellar masses that are compatible with the seismic data. RGB models with $1\,M_\odot$ are too cool for [Fe/H] = 0.17 by about 200 K or, conversely, too metal-rich for the observed effective temperature by about 0.35 dex. The temperature difference between the RC and the RGB at fixed $\log g$ is smaller for tracks of larger masses, as the effective temperature of the clump does not change while that of the RGB gets higher. Our grid-based modeling for the RGB scenario reflects this, yielding a higher mass, around $1.2\,M_\odot$. This higher mass is obtained at the expense of a posterior $\nu_{\max}$ higher than, and in tension with, the observed value. Finally, it is worth mentioning that this conclusion is robust against the temperature scale defined by the choice of mixing length, α_{MLT}, in the stellar models. We tested models with α_{MLT} ranging from 1.8 (solar-calibrated value with an Eddington atmosphere) to 2.1 (solar-calibrated value with a Krishna Swamy atmosphere), with almost no impact on the Bayes' factor, which varied from 75 for $\alpha_{\mathrm{MLT}} = 1.8$ down to 70 for $\alpha_{\mathrm{MLT}} = 2.1$.

We have also employed the Bayesian inference method of Stock et al. (2018). This method compares the position of a star in the Hertzsprung–Russell diagram with those of the latest PARSEC evolutionary models (Bressan et al. 2012). The spectroscopically determined metallicity, $B - V$ color, and astrometry-based luminosity (Arenou & Luri 1999), computed from the adjusted *Gaia* parallax in Table 2, were used as constraints. Moreover, the initial mass function and the evolutionary timescale at each model position were used as priors in the Bayesian inference. The outcomes are probability density functions for the stellar parameters as well as probabilities of the star being either on the RGB or the horizontal branch. The method was carefully tested by Stock et al. (2018) against reference samples with accurate stellar parameters determined using different methods, and was found to deliver very reliable results. In particular, its reliability was tested against a sample of evolved stars with evolutionary states determined from asteroseismology, resulting in an accuracy of 86%. Application of this method returns a probability of HD 203949 being an RC star of $p = 0.93$.

Asymptotic Acoustic-Mode Offset. Kallinger et al. (2012) found an empirical relation between the asymptotic offset, ϵ_c, of radial modes in red giants and the evolutionary state, separating H-shell (RGB) from He-core burning stars. Christensen-Dalsgaard et al. (2014) provided a theoretical interpretation of this relation, which was found to derive from differences in the thermodynamic state of the convective envelope. Both works acknowledge the potential of this relation for distinguishing RGB and clump stars when faced with observations that are too short to allow such a distinction based on the determination of $\Delta\Pi_1$. We extracted frequencies[42] from the PSD of HD 203949 using the multi-modal approach described in Corsaro (2019). The value of ϵ_c was then constrained from an échelle diagram and found to be 1.24 ± 0.05. The quoted uncertainty corresponds to the width of the expected $\ell = 0$ ridge in the échelle diagram and reflects the lack of resolving power to properly disentangle radial modes from adjacent quadrupole modes. We note, however, that this uncertainty is not consistent with the one in $\Delta\nu$ and should thus be considered as a lower limit. An uncertainty of 0.05 in ϵ_c translates into a relative uncertainty in $\Delta\nu$ of about $0.05/n_{\max} < 1\%$ (e.g., Mosser et al. 2013), with $n_{\max}$ the radial order at $\nu_{\max}$. Table 2 nevertheless quotes a relative uncertainty in $\Delta\nu$ of 3.4%. Once the uncertainty in ϵ_c has been calibrated, the measured value of $\epsilon_c = 1.2 \pm 0.2$ then allows for both evolutionary states (within 1.5σ) in the top panel of Figure 4 of Kallinger et al. (2012).

Spectroscopic evolutionary state. We made an attempt at inferring the spectroscopic evolutionary state of HD 203949 as described in Holtzman et al. (2018). The basic idea behind this approach is to use a ridgeline in the T_{eff}–$\log g$ plane that is a function of metallicity, and supplement this with a measurement of the surface [C/N] ratio, as the latter is expected (and observed) to further separate the RGB and RC. This approach was devised to separate RGB and RC stars in the (asteroseismic) APOKASC sample (Pinsonneault et al. 2018) and has an accuracy of approximately 95%. In the absence of a [C/N] measurement, we estimated the range of possible values from the stellar mass, taking as reference the APOKASC sample. This led to the star being most likely in the RC. However, we also have to account for the fact that the above

---

[42] Note that these frequencies are not obtained from a full peak-bagging analysis. Nevertheless, they are still reliable and match observed peaks in the PSD.

relations are defined in the APOKASC sample only and that there could be a systematic offset between the T_{eff} and/or metallicity scales. To test this, we computed the photometric temperature by means of the infrared flux method (González Hernández & Bonifacio 2009), leading to a temperature cooler than the spectroscopic one (at the 1.5σ level). Adopting the photometric temperature, one instead arrived at the RGB classification. The issue of evolutionary state hence seems to rely sensitively on the effective temperature, given that the error on the spectroscopic T_{eff} is large enough to encompass both scenarios.

In summary, all but one approach give an ambiguous answer. The spectroscopic evolutionary state is unresolved due to the possibility of a systematic offset between the T_{eff} scales. The asymptotic acoustic-mode offset, ϵ_c, whose uncalibrated uncertainty is a poorly constrained lower limit, allows for both evolutionary states. Despite its inconclusiveness in this particular instance, machine-learning classification still exhibits a high degree of accuracy, thus holding great promise for large ensemble studies with *TESS* (e.g., Galactic archaeology). Finally, the two applications of grid-based modeling provide very strong evidence in support of the RC scenario given the adopted set of seismic and spectroscopic constraints. Although the balance of evidence seems to favor the RC scenario, there are two points worth noting. First, there has been rising concern that standard RC models might suffer from important underlying systematic errors (e.g., An et al. 2019), which could undermine results coming out from the grid-based modeling approach. Second, there is no direct observational evidence decisively pointing to either scenario. In light of the above, we thus refrain from providing a definitive classification of the evolutionary state of HD 203949.

5.3. Orbital Evolution of HD 203949 b: Avoiding Engulfment at the Tip of the RGB

The history, evolution and fate of the planet orbiting HD 203949 change significantly depending on whether the star is an RGB or a RC star. The more straightforward scenario is that HD 203949 is in the process of ascending the RGB and will eventually engulf the orbiting planet. The alternative scenario, in which HD 203949 is in the RC, calls for a more detailed examination. We now go on to discuss this scenario.

The variations in radius, luminosity, and mass of giant-branch stars often have destructive consequences for planetary systems (Veras 2016). Most important for HD 203949 b is the radius variation of the host star, which could incite star–planet tides that might engulf the planet (Villaver & Livio 2009; Kunitomo et al. 2011; Mustill & Villaver 2012; Adams & Bloch 2013; Nordhaus & Spiegel 2013; Valsecchi & Rasio 2014; Villaver et al. 2014; Madappatt et al. 2016; Staff et al. 2016; Gallet et al. 2017; Rao et al. 2018). The asteroseismic stellar mass of $1.00 \pm 0.16\,M_\odot$ (under the clump assumption) would tidally influence and probably lead to the engulfment and destruction of a Jovian planet on a 184 days orbit at the tip of the RGB.

A planet which is engulfed in the low-density atmosphere of a giant-branch star usually decays quickly enough for it to be considered destroyed. Figure 4 of MacLeod et al. (2018) estimates decay times of engulfed Jovian planets across the Hertzsprung–Russell diagram, and finds that the spiral-in process lasts 10^0–10^4 orbits. The upper bound of this range (corresponding to about 5000 yr in our case) is much less than

the timescale (about 2 Myr) in which this star's radius would exceed a (0.63 au) during the RGB phase. Hence, HD 203949 b would unlikely have survived being engulfed.

Now let us assume that the planet would avoid being engulfed. In general, there are two outcomes: (1) the outward expansion of the planet's orbit due to stellar mass loss dominates over tidal effects, and the planet's final semimajor axis increases, or (2) tidal effects dominate over mass loss, but only for a short enough time to prevent engulfment, leading to a decrease in the final semimajor axis. Outcome (2) is expected to be rare because the engulfment timescale is so small. Nevertheless, this outcome may explain the current orbit of HD 203949 b under the clump assumption.

We explored this possibility by performing numerical simulations of star–planet tides, with the intention of providing rough estimates.[43] We used four different stellar tracks with different values of the Reimers' mass-loss coefficient, η, metallicity and atmospheric type (Krishna Swamy and Eddington, which lead to different model T_{eff} scales on the RGB and hence different stellar radii), which fit the currently measured stellar observables. In all cases, a planetary semimajor axis corresponding to a 184 days period (0.63 au) is well within the maximal radial extent of the star, which is attained at the tip of the RGB and ranges from 0.85 to 0.99 au across the four tracks. Therefore, outcome (2) from above would apply to this system.

The extent to which the planet would be dragged inward changes depending on the details of the tidal formalism adopted. We used a basic formulation of dynamical tides from Zahn (1977), as implemented in Villaver et al. (2014), by (i) including frictional forces from the stellar envelope, (ii) adopting velocity and density prescriptions from Equations (53) and (54) of Veras et al. (2015), (iii) assuming zero eccentricity throughout the simulation, (iv) assuming a planetary radius of $1.0\,R_J$, and (v) assuming adiabatic stellar mass loss, which is a robust approximation for this system (Veras et al. 2011).

In order for the planet to achieve an orbit with a semimajor axis of 0.6–1.0 au, we hence find that the main-sequence semimajor axis of the planet would have resided within an extremely narrow range (an interval much smaller than 10^{-2} au) centered on a specific value within the interval 3.1–3.5 au (which is set by the stellar model adopted and details of the tidal prescription). This result makes sense in the context of, for example, Figures 1, 4, and 6 of Villaver et al. (2014).

A different, but also viable explanation for the current 0.63 au orbit would be for the planet to have been gravitationally scattered into its current position after the host star had reached the tip of the RGB.[44] Although RGB mass loss might have triggered the instability leading to this scenario (Debes & Sigurdsson 2002; Veras et al. 2013), more recent suites of simulations of multiple giant-planet systems demonstrate that post-mass-loss scattering events—at least for single stars[45]—are usually delayed until the white dwarf phase (Mustill et al. 2014, 2018; Veras & Gänsicke 2015; Veras

---

[43] Not considered here are the effects of evaporation of the planet's atmosphere due to the RGB stellar luminosity.

[44] Some tidal circularization might have followed the scattering event, as scattering alone usually excites rather than damps orbital eccentricity.

[45] Jones et al. (2014) did detect a long-term linear trend in the RV residuals, which might be attributed to the presence of a distant stellar companion. However, no constraints were placed on the mass nor orbital period of this putative companion.

et al. 2016, 2018). Increasing the feasibility of gravitational scattering is that those studies adopted more massive stars than HD 203949, and hence would harbor shorter giant-branch lifetimes in which scattering could occur.

6. Outlook

Characterization of host stars is a critical component of understanding their planets. For example, the radius of the star is required to estimate the radius of the planet from transit observations, and the luminosity and effective temperature of the star are crucial ingredients for determining the incident flux received by the planet and the extent of the Habitable Zone (Kane 2014; Kane et al. 2016). For known systems observed with *TESS*, the combination of precision photometry with asteroseismology will aid in the assessment of potential transit events for RV planets (Dalba et al. 2019). Dynamical studies of planetary systems require detailed knowledge of the stellar properties, such as the stellar mass (Menou & Tabachnik 2003). Furthermore, the evolution of orbits as stars move off the main sequence depends on the stellar mass and radius, as these relate to the mass loss relative to the progenitor (Damiani & Mathis 2018). Additionally, the angular size of the host star will be invaluable information when considering known systems as potential direct imaging targets (Kane et al. 2018). Finally, accurate stellar radii for evolved stars will greatly improve transit probability estimates. Transit probabilities for evolved stars tend to have the largest values, because they scale linearly with stellar radius (Kane et al. 2010). The asteroseismology techniques described here are thus an important component of overall planetary system characterization.

ORCID iDs

Tiago L. Campante ● https://orcid.org/0000-0002-4588-5389
Enrico Corsaro ● https://orcid.org/0000-0001-8835-2075
Mikkel N. Lund ● https://orcid.org/0000-0001-9214-5642
Benoît Mosser ● https://orcid.org/0000-0002-7547-1208
Aldo Serenelli ● https://orcid.org/0000-0001-6359-2769
Dimitri Veras ● https://orcid.org/0000-0001-8014-6162
Vardan Adibekyan ● https://orcid.org/0000-0002-0601-6199
H. M. Antia ● https://orcid.org/0000-0001-7549-9684
Warrick Ball ● https://orcid.org/0000-0002-4773-1017
Sarbani Basu ● https://orcid.org/0000-0002-6163-3472
Timothy R. Bedding ● https://orcid.org/0000-0001-5222-4661
Diego Bossini ● https://orcid.org/0000-0002-9480-8400
Guy R. Davies ● https://orcid.org/0000-0002-4290-7351
Elisa Delgado Mena ● https://orcid.org/0000-0003-4434-2195
Rafael A. García ● https://orcid.org/0000-0002-8854-3776
Rasmus Handberg ● https://orcid.org/0000-0001-8725-4502
Marc Hon ● https://orcid.org/0000-0003-2400-6960
Stephen R. Kane ● https://orcid.org/0000-0002-7084-0529
Steven D. Kawaler ● https://orcid.org/0000-0002-6536-6367
James S. Kuszlewicz ● https://orcid.org/0000-0002-3322-5279
Savita Mathur ● https://orcid.org/0000-0002-0129-0316
Nicolas Nardetto ● https://orcid.org/0000-0002-7399-0231
Martin B. Nielsen ● https://orcid.org/0000-0001-9169-2599
Marc H. Pinsonneault ● https://orcid.org/0000-0002-7549-7766
Sabine Reffert ● https://orcid.org/0000-0002-0460-8289
Víctor Silva Aguirre ● https://orcid.org/0000-0002-6137-903X
Keivan G. Stassun ● https://orcid.org/0000-0002-3481-9052

Dennis Stello (ORCID) https://orcid.org/0000-0002-4879-3519
Stephan Stock (ORCID) https://orcid.org/0000-0002-1166-9338
Mutlu Yıldız (ORCID) https://orcid.org/0000-0002-7772-7641
William J. Chaplin (ORCID) https://orcid.org/0000-0002-5714-8618
Daniel Huber (ORCID) https://orcid.org/0000-0001-8832-4488
Jacob L. Bean (ORCID) https://orcid.org/0000-0003-4733-6532
Zeynep Çelik Orhan (ORCID) https://orcid.org/0000-0002-9424-2339
Margarida S. Cunha (ORCID) https://orcid.org/0000-0001-8237-7343
Jørgen Christensen-Dalsgaard (ORCID) https://orcid.org/0000-0001-5137-0966
Hans Kjeldsen (ORCID) https://orcid.org/0000-0002-9037-0018
Travis S. Metcalfe (ORCID) https://orcid.org/0000-0003-4034-0416
Andrea Miglio (ORCID) https://orcid.org/0000-0001-5998-8533
Mário J. P. F. G. Monteiro (ORCID) https://orcid.org/0000-0003-0513-8116
Benard Nsamba (ORCID) https://orcid.org/0000-0002-4647-2068
Sibel Örtel (ORCID) https://orcid.org/0000-0001-5759-7790
Filipe Pereira (ORCID) https://orcid.org/0000-0002-2157-7146
Sérgio G. Sousa (ORCID) https://orcid.org/0000-0001-9047-2965
Maria Tsantaki (ORCID) https://orcid.org/0000-0002-0552-2313

References

Adams, F. C., & Bloch, A. M. 2013, ApJL, 777, L30
Adibekyan, V., Figueira, P., Santos, N. C., et al. 2015a, A&A, 583, A94
Adibekyan, V. Z., Benamati, L., Santos, N. C., et al. 2015b, MNRAS, 450, 1900
Adibekyan, V. Z., Sousa, S. G., Santos, N. C., et al. 2012, A&A, 545, A32
An, D., Pinsonneault, M. H., Terndrup, D. M., & Chung, C. 2019, ApJ, 879, 81
Arenou, F., & Luri, X. 1999, in ASP Conf. Ser. 167, Harmonizing Cosmic Distance Scales in a Post-HIPPARCOS Era, ed. D. Egret & A. Heck (San Francisco, CA: ASP), 13
Arentoft, T., Grundahl, F., White, T. R., et al. 2019, A&A, 622, A190
Bae, J., Ryu, Y., Chang, T., Song, I., & Kim, H. M. 1996, SigPr, 52, 75
Baglin, A., Auvergne, M., Barge, P., et al. 2009, in IAU Symp. 253, Transiting Planets, ed. F. Pont, D. Sasselov, & M. J. Holman (Cambridge: Cambridge Univ. Press), 71
Bailer-Jones, C. A. L., Rybizki, J., Fouesneau, M., Mantelet, G., & Andrae, R. 2018, AJ, 156, 58
Ballard, S., Chaplin, W. J., Charbonneau, D., et al. 2014, ApJ, 790, 12
Basu, S., Chaplin, W. J., & Elsworth, Y. 2010, ApJ, 710, 1596
Basu, S., Verner, G. A., Chaplin, W. J., & Elsworth, Y. 2012, ApJ, 746, 76
Belkacem, K., Goupil, M. J., Dupret, M. A., et al. 2011, A&A, 530, A142
Borucki, W. J., Koch, D., Basri, G., et al. 2010, Sci, 327, 977
Bressan, A., Marigo, P., Girardi, L., et al. 2012, MNRAS, 427, 127
Brown, T. M., Gilliland, R. L., Noyes, R. W., & Ramsey, L. W. 1991, ApJ, 368, 599
Campante, T. L. 2018, in Asteroseismology and Exoplanets: Listening to the Stars and Searching for New Worlds, ed. T. L. Campante, N. Santos, & M. Monteiro (Cham: Springer), 55
Campante, T. L., Barclay, T., Swift, J. J., et al. 2015, ApJ, 799, 170
Campante, T. L., Lund, M. N., Kuszlewicz, J. S., et al. 2016a, ApJ, 819, 85
Campante, T. L., Santos, N. C., & Monteiro, M. J. P. F. G. 2018, Asteroseismology and Exoplanets: Listening to the Stars and Searching for New Worlds (Cham: Springer)
Campante, T. L., Schofield, M., Kuszlewicz, J. S., et al. 2016b, ApJ, 830, 138
Campante, T. L., Veras, D., North, T. S. H., et al. 2017, MNRAS, 469, 1360
Capitanio, L., Lallement, R., Vergely, J. L., Elyajouri, M., & Monreal-Ibero, A. 2017, A&A, 606, A65
Chaplin, W. J., & Miglio, A. 2013, ARA&A, 51, 353
Chaplin, W. J., Sanchis-Ojeda, R., Campante, T. L., et al. 2013, ApJ, 766, 101
Chen, T., & Guestrin, C. 2016, arXiv:1603.02754
Christensen-Dalsgaard, J., Silva Aguirre, V., Elsworth, Y., & Hekker, S. 2014, MNRAS, 445, 3685
Corsaro, E. 2019, FrASS, 6, 21
Corsaro, E., & De Ridder, J. 2014, A&A, 571, A71
Corsaro, E., De Ridder, J., & García, R. A. 2015, A&A, 579, A83
Corsaro, E., Mathur, S., García, R. A., et al. 2017, A&A, 605, A3
Cutri, R. M., Skrutskie, M. F., van Dyk, S., et al. 2003, yCat, 2246

Dalba, P. A., Kane, S. R., Barclay, T., et al. 2019, PASP, 131, 034401
Damiani, C., & Mathis, S. 2018, A&A, 618, A90
Davies, G. R., Handberg, R., Miglio, A., et al. 2014, MNRAS, 445, L94
Davies, G. R., & Miglio, A. 2016, AN, 337, 774
Davies, G. R., Silva Aguirre, V., Bedding, T. R., et al. 2016, MNRAS, 456, 2183
Debes, J. H., & Sigurdsson, S. 2002, ApJ, 572, 556
Deheuvels, S., Doğan, G., Goupil, M. J., et al. 2014, A&A, 564, A27
Gai, N., Basu, S., Chaplin, W. J., & Elsworth, Y. 2011, ApJ, 730, 63
Gaia Collaboration, Brown, A. G. A., Vallenari, A., et al. 2018, A&A, 616, A1
Gallenne, A., Pietrzyński, G., Graczyk, D., et al. 2018, A&A, 616, A68
Gallet, F., Bolmont, E., Mathis, S., Charbonnel, C., & Amard, L. 2017, A&A, 604, A112
González Hernández, J. I., & Bonifacio, P. 2009, A&A, 497, 497
Gould, B. A. 1855, AJ, 4, 81
Goupil, M. J., Mosser, B., Marques, J. P., et al. 2013, A&A, 549, A75
Green, G. M., Schlafly, E. F., Finkbeiner, D. P., et al. 2015, ApJ, 810, 25
Handberg, R., & Lund, M. N. 2014, MNRAS, 445, 2698
Handberg, R., & Lund, M. N. 2018, T'DA Data Release Notes—Data Release 3 for TESS Sectors 1 + 2, Version TASOC-0003-02, Zenodo, doi:10.5281/zenodo.2510028
Hekker, S., Elsworth, Y., De Ridder, J., et al. 2011, A&A, 525, A131
Høg, E., Fabricius, C., Makarov, V. V., et al. 2000, A&A, 355, L27
Holtzman, J. A., Hasselquist, S., Shetrone, M., et al. 2018, AJ, 156, 125
Hon, M., Stello, D., & Yu, J. 2017, MNRAS, 469, 4578
Hon, M., Stello, D., & Yu, J. 2018, MNRAS, 476, 3233
Houk, N. 1982, Michigan Catalogue of Two-dimensional Spectral Types for the HD Stars. Volume 3, Declinations −40°0 to −26°0 (Ann Arbor, MI: Univ. Michigan Press)
Houk, N., & Smith-Moore, M. 1988, Michigan Catalogue of Two-dimensional Spectral Types for the HD Stars. Volume 4, Declinations −26°0 to −12°0 (Ann Arbor, MI: Univ. Michigan Press)
Howell, S. B., Sobeck, C., Haas, M., et al. 2014, PASP, 126, 398
Huber, D. 2018, in Asteroseismology and Exoplanets: Listening to the Stars and Searching for New Worlds, ed. T. Campante, N. Santos, & M. Monteiro (Cham: Springer), 119
Huber, D., Bedding, T. R., Stello, D., et al. 2011, ApJ, 743, 143
Huber, D., Carter, J. A., Barbieri, M., et al. 2013b, Sci, 342, 331
Huber, D., Chaplin, W. J., Chontos, A., et al. 2019, AJ, 157, 245
Huber, D., Chaplin, W. J., Christensen-Dalsgaard, J., et al. 2013a, ApJ, 767, 127
Huber, D., Stello, D., Bedding, T. R., et al. 2009, CoAst, 160, 74
Jenkins, J. M., Twicken, J. D., McCauliff, S., et al. 2016, Proc. SPIE, 9913, 99133E
Jofré, E., Petrucci, R., Saffe, C., et al. 2015, A&A, 574, A50
Johnson, J. A., Fischer, D. A., Marcy, G. W., et al. 2007, ApJ, 665, 785
Johnson, J. A., Howard, A. W., Bowler, B. P., et al. 2010, PASP, 122, 701
Jones, M. I., Jenkins, J. S., Bluhm, P., Rojo, P., & Melo, C. H. F. 2014, A&A, 566, A113
Jones, M. I., Jenkins, J. S., Rojo, P., & Melo, C. H. F. 2011, A&A, 536, A71
Kallinger, T., De Ridder, J., Hekker, S., et al. 2014, A&A, 570, A41
Kallinger, T., Hekker, S., Mosser, B., et al. 2012, A&A, 541, A51
Kamiaka, S., Benomar, O., & Suto, Y. 2018, MNRAS, 479, 391
Kamiaka, S., Benomar, O., Suto, Y., et al. 2019, AJ, 157, 137
Kane, S. R. 2014, ApJ, 782, 111
Kane, S. R., Hill, M. L., Kasting, J. F., et al. 2016, ApJ, 830, 1
Kane, S. R., Meshkat, T., & Turnbull, M. C. 2018, AJ, 156, 267
Kane, S. R., Reffert, S., Henry, G. W., et al. 2010, ApJ, 720, 1644
Kedem, B., & Slud, E. 1981, Biometrika, 68, 551
Kedem, B., & Slud, E. 1982, AnSta, 10, 786
Kjeldsen, H., & Bedding, T. R. 1995, A&A, 293, 87
Kjeldsen, H., Bedding, T. R., Arentoft, T., et al. 2008, ApJ, 682, 1370
Kjeldsen, H., Bedding, T. R., Butler, R. P., et al. 2005, ApJ, 635, 1281
Koch, D. G., Borucki, W. J., Basri, G., et al. 2010, ApJL, 713, L79
Kunitomo, M., Ikoma, M., Sato, B., Katsuta, Y., & Ida, S. 2011, ApJ, 737, 66
Kurucz, R. L. 2013, ATLAS12: Opacity sampling model atmosphere program, 1303, 024
Lallement, R., Vergely, J.-L., Valette, B., et al. 2014, A&A, 561, A91
Lund, M. N. 2019, MNRAS, 489, 1072
Lund, M. N., Handberg, R., Davies, G. R., Chaplin, W. J., & Jones, C. D. 2015, ApJ, 806, 30
Lund, M. N., Handberg, R., Kjeldsen, H., Chaplin, W. J., & Christensen-Dalsgaard, J. 2017a, EPJWC, 160, 01005
Lund, M. N., Silva Aguirre, V., Davies, G. R., et al. 2017b, ApJ, 835, 172
Lundkvist, M. S., Kjeldsen, H., Albrecht, S., et al. 2016, NatCo, 7, 11201
MacLeod, M., Cantiello, M., & Soares-Furtado, M. 2018, ApJL, 853, L1

Madappatt, N., De Marco, O., & Villaver, E. 2016, MNRAS, 463, 1040
Mathur, S., García, R. A., Régulo, C., et al. 2010, A&A, 511, A46
Mathur, S., Metcalfe, T. S., Woitaszek, M., et al. 2012, ApJ, 749, 152
Menou, K., & Tabachnik, S. 2003, ApJ, 583, 473
Metcalfe, T. S., Monteiro, M. J. P. F. G., Thompson, M. J., et al. 2010, ApJ, 723, 1583
Mosser, B., & Appourchaux, T. 2009, A&A, 508, 877
Mosser, B., Belkacem, K., Goupil, M. J., et al. 2011, A&A, 525, L9
Mosser, B., Benomar, O., Belkacem, K., et al. 2014, A&A, 572, L5
Mosser, B., Gehan, C., Belkacem, K., et al. 2018, A&A, 618, A109
Mosser, B., Goupil, M. J., Belkacem, K., et al. 2012, A&A, 540, A143
Mosser, B., Michel, E., Belkacem, K., et al. 2013, A&A, 550, A126
Mosser, B., Pinçon, C., Belkacem, K., Takata, M., & Vrard, M. 2017, A&A, 600, A1
Mosser, B., Vrard, M., Belkacem, K., Deheuvels, S., & Goupil, M. J. 2015, A&A, 584, A50
Mustill, A. J., Veras, D., & Villaver, E. 2014, MNRAS, 437, 1404
Mustill, A. J., & Villaver, E. 2012, ApJ, 761, 121
Mustill, A. J., Villaver, E., Veras, D., Gänsicke, B. T., & Bonsor, A. 2018, MNRAS, 476, 3939
Nishiyama, S., Tamura, M., Hatano, H., et al. 2009, ApJ, 696, 1407
Nordhaus, J., & Spiegel, D. S. 2013, MNRAS, 432, 500
North, T. S. H., Campante, T. L., Miglio, A., et al. 2017, MNRAS, 472, 1866
Nsamba, B., Campante, T. L., Monteiro, M. J. P. F. G., et al. 2018, MNRAS, 477, 5052
Peirce, B. 1852, AJ, 2, 161
Pietrzyński, G., Graczyk, D., Gallenne, A., et al. 2019, Natur, 567, 200
Pinsonneault, M. H., Elsworth, Y. P., Tayar, J., et al. 2018, ApJS, 239, 32
Rao, S., Meynet, G., Eggenberger, P., et al. 2018, A&A, 618, A18
Rauer, H., Catala, C., Aerts, C., et al. 2014, ExA, 38, 249
Rendle, B. M., Buldgen, G., Miglio, A., et al. 2019, MNRAS, 484, 771
Ricker, G. R., Winn, J. N., Vanderspek, R., et al. 2015, JATIS, 1, 014003
Rodrigues, T. S., Bossini, D., Miglio, A., et al. 2017, MNRAS, 467, 1433
Rodrigues, T. S., Girardi, L., Miglio, A., et al. 2014, MNRAS, 445, 2758
Santos, N. C., Sousa, S. G., Mortier, A., et al. 2013, A&A, 556, A150
Schlegel, D. J., Finkbeiner, D. P., & Davis, M. 1998, ApJ, 500, 525

Schofield, M., Chaplin, W. J., Huber, D., et al. 2019, ApJS, 241, 12
Serenelli, A., Johnson, J., Huber, D., et al. 2017, ApJS, 233, 23
Silva Aguirre, V., Davies, G. R., Basu, S., et al. 2015, MNRAS, 452, 2127
Silva Aguirre, V., Lund, M. N., Antia, H. M., et al. 2017, ApJ, 835, 173
Sliski, D. H., & Kipping, D. M. 2014, ApJ, 788, 148
Sousa, S. G., Adibekyan, V., Delgado-Mena, E., et al. 2018, A&A, 620, A58
Staff, J. E., De Marco, O., Wood, P., Galaviz, P., & Passy, J.-C. 2016, MNRAS, 458, 832
Stassun, K. G., Corsaro, E., Pepper, J. A., & Gaudi, B. S. 2018a, AJ, 155, 22
Stassun, K. G., Oelkers, R. J., Pepper, J., et al. 2018b, AJ, 156, 102
Stassun, K. G., & Torres, G. 2016, AJ, 152, 180
Stassun, K. G., & Torres, G. 2018, ApJ, 862, 61
Stello, D., Chaplin, W. J., Bruntt, H., et al. 2009, ApJ, 700, 1589
Stock, S., Reffert, S., & Quirrenbach, A. 2018, A&A, 616, A33
Valsecchi, F., & Rasio, F. A. 2014, ApJ, 786, 102
Van Eylen, V., & Albrecht, S. 2015, ApJ, 808, 126
Van Eylen, V., Albrecht, S., Huang, X., et al. 2019, AJ, 157, 61
van Leeuwen, F. 2007, A&A, 474, 653
Veras, D. 2016, RSOS, 3, 150571
Veras, D., Eggl, S., & Gänsicke, B. T. 2015, MNRAS, 451, 2814
Veras, D., & Gänsicke, B. T. 2015, MNRAS, 447, 1049
Veras, D., Georgakarakos, N., Gänsicke, B. T., & Dobbs-Dixon, I. 2018, MNRAS, 481, 2180
Veras, D., Mustill, A. J., Bonsor, A., & Wyatt, M. C. 2013, MNRAS, 431, 1686
Veras, D., Mustill, A. J., Gänsicke, B. T., et al. 2016, MNRAS, 458, 3942
Veras, D., Wyatt, M. C., Mustill, A. J., Bonsor, A., & Eldridge, J. J. 2011, MNRAS, 417, 2104
Verner, G. A., Elsworth, Y., Chaplin, W. J., et al. 2011, MNRAS, 415, 3539
Villaver, E., & Livio, M. 2009, ApJL, 705, L81
Villaver, E., Livio, M., Mustill, A. J., & Siess, L. 2014, ApJ, 794, 3
Vrard, M., Mosser, B., & Samadi, R. 2016, A&A, 588, A87
Yıldız, M., Çelik Orhan, Z., & Kayhan, C. 2016, MNRAS, 462, 1577
Yu, J., Huber, D., Bedding, T. R., et al. 2018, ApJS, 236, 42
Zahn, J. P. 1977, A&A, 500, 121